Epsilon Cobalt Nanoparticles as Highly Performant Catalysts in Cinnamaldehyde Selective Hydrogenation

Deliang Yi, Yuanyuan Min, Beatrice Muzzi, Audrey Marty, Idaline Romana, Pier-Francesco Fazzini, Thomas Blon, Guillaume Viau, Philippe Serp, Katerina Soulantica

Epsilon Cobalt Nanoparticles as Highly Performant Catalysts in Cinnamaldehyde Selective Hydrogenation

Deliang Yi[1,2], Yuanyuan Min[1], Beatrice Muzzi[1], Audrey Marty[1], Idaline Romana[2], Pier-Francesco Fazzini[1], Thomas Blon[1], Guillaume Viau[1], Philippe Serp[2] and Katerina Soulantica[1]**

1. Université de Toulouse, LPCNO CNRS, INSA, UPS UMR 5215, 31077 Toulouse, France;
2. LCC, CNRS-UPR 8241, ENSIACET, Université de Toulouse, France

Abstract

Epsilon cobalt nanoparticles are under-explored in catalysis due to the fact that they are accessible only through wet-chemical approaches which employ ligands as stabilizing agents. Ligands may play a significant role in determining the structure and the catalytic performances of nanoparticles, which complicates their comparison in catalysis. Here we present the catalytic performances in cinnamaldehyde hydrogenation, of freestanding and few-layer graphene-supported ε-Co nanoparticles and *hcp*-Co nanorods which are stabilized by the same ligands. We show that while *hcp*-Co nanorods exposing a majority of {11-20} type facets are the most active, the supported spherical ε-Co nanoparticles combine high activity and excellent selectivity for the selective hydrogenation of cinnamaldehyde to cinnamyl alcohol. The concentration dependent ligand conformation on the surface of the nanostructures influences their catalytic performances with higher concentrations favoring both activity and selectivity to cinnamyl alcohol. These results should incite the interest in the implementation of ε-Co nanoparticles in other catalytic reactions where the cobalt crystal structure may play an important role.

Keywords: hcp-cobalt, epsilon-cobalt, nanoparticles, selective hydrogenation, ligands

Introduction

Cobalt nanoparticles (Co_{NP}) present physical and chemical properties exploitable in many applications.[1-4] These properties critically depend on NP structural features such as size and shape. The type of facets exposed by the nanocrystals depends on their morphology, which is highly dependent on the crystal structure. Co_{NP} can adopt three crystallographic structures: hexagonal close packed *(hcp*), face centered cubic (*fcc*) and epsilon (ε).[5] The ε-phase has been unambiguously identified and fully characterized only recently for Co_{NP} prepared by liquid phase synthesis.[6,7]

Crystal structure dependent catalytic performances have been demonstrated in several cases where allotropes were available for comparison.[8,9] For instance, *hcp* and *fcc* Ru nanostructures show different performances in catalytic reactions such as the hydrogenation of arenes and substituted arenes.[10,11] In another example of rarer nanoalloy allotropes, PdCu nanoalloys of *fcc* and body centered cubic (*bcc*) structures have shown different selectivities in the hydrodeoxygenation of 5-hydroxymethylfurfural. [12] For the case of Co it has been shown that the Co crystal phase (*hcp* or *fcc*) impacts the catalytic performances in Fischer-Tropsch Synthesis (FTS),[13,14] On the other hand, the ε-Co phase is practically absent from dedicated studies.[15] This is in part due to the fact that ε-Co is metastable,[5] and can be converted to the other two phases upon thermal treatments prior to catalyst use, or under the catalytic reaction conditions. Furthermore, ε-Co can only be obtained by colloidal syntheses, which are rarely employed in heterogeneous catalyst preparation methods. While conventional elaboration of supported catalysts allows only a limited degree of control over size, shape and crystal structure of the active phase, colloidal methods are well adapted for the synthesis of nanocrystals of well-controlled features that can be advantageously exploited in several catalytic reactions.[16,17] For structure-sensitive catalytic reactions, and provided that the reaction conditions do not induce significant structural modifications of the catalytically active phase, colloidal NPs can contribute to a better rationalization of catalytic processes, and to the development of efficient catalytic systems.[18] Nevertheless, colloidal NPs invariably comprise capping agents (ligands), which not only stabilize them, but they also play a determinant role in controlling NP nucleation and growth steps, thus dictating their structure (size, shape, crystal structure). NPs of the same material but adopting different structures (phase, shape) are generally stabilized by different ligands, and ligand elimination is in general accompanied by modification of the NPs features. Ligand influence on the performances of NP-based catalysts is multifaceted and

controversial.[19-23] Thus, the study of the influence of the structural characteristics of colloidal NPs on their catalytic properties is always hampered by the presence of ligands.

The chemoselective reduction of ketones/aldehydes is a widely used, fundamental reaction in organic chemistry.[19] In particular, the selective hydrogenation of α,β-unsaturated aldehydes, among which cinnamaldehyde (CAL), is an industrially relevant reaction for producing high added value chemicals through hydrogenation of either the C=O or the C=C bond. CAL can be hydrogenated via two parallel reactions to (i) hydrocinnamaldehyde (HCAL) through C=C hydrogenation, and (ii) cinnamyl alcohol (COL) through C=O hydrogenation. Further hydrogenation yields the fully hydrogenated 3-phenyl-1-propanol (HCOL) (insert in Table 1). The easier hydrogenation of the C=C bond by the most widespread hydrogenation catalysts (Pt, Pd, Ru, Ni) has incited the development of COL-selective catalysts, through introduction of elements that can appropriately modify the properties of the basic metal.[24,25] However, the high price and the scarcity of the most active hydrogenation metals (Pd, Pt) urges for more sustainable alternatives. Among the cost-effective metals, cobalt has been used as a COL selectivity promoter of Pt based-catalysts.[26-29] Nevertheless, when employed alone, while more selective, it is not a viable catalyst because of its low activity. Thus, examples of cobalt-based catalysts for the selective hydrogenation of α,β -unsaturated alcohols are rather scarce and among them, only very few concern pure Co.[30-41] The development of a stable, active and COL-selective pure cobalt catalyst would thus, be a major breakthrough in the field.

Size-, shape- and crystal structure-controlled cobalt nanostructures have been synthesized by some of us by the reduction by H_2 of $[Co\{N(SiMe_3)_2\}_2(thf)]$ in the presence of lauric acid (LA) and hexadecylamine (HDA).[42,43] The as-prepared Co nano-objects are purely metallic, thus, no reductive post-treatments prone to modify their structural characteristics are needed prior to their implementation, as recently shown in the case of FTS[44,45] and in the acceptorless dehydrogenation of 2-octanol.[46]

Here, we present the performances in the chemoselective hydrogenation of CAL of two types of nano-objects, formed simultaneously in the same synthesis: *hcp* Co nanorods (*hcp*-Co_{NR}) exposing mainly $\{11\bar{2}0\}$ type facets and isotropic ε-Co_{NP}. We show that while *hcp*-Co_{NR} are more active, ε-Co_{NP} supported on functionalized few-layer graphene are also active and by far the most selective cobalt catalysts for COL production, reported so far.

Experimental Section

Materials

Due to the air-sensitivity of the cobalt precursor and the cobalt nanocrystals, all manipulations have been performed under inert conditions, either by using standard Schlenk techniques or in a glove box. Hexadecylamine (HDA, 98%, Aldrich) and lauric acid (LA, 99 %, Acros) were transferred in the glovebox and used without further purification. Toluene (99 %, Fisher) was purified by a solvent purifier (Innovative Technology Purification System) and stocked in the glovebox. 1,4-dioxane (100 %, VWR Chemicals), cinnamaldehyde (97 %, Aldrich), nonane (99 %, Sigma-Aldrich), ethanol (dried, 99.9 %, Seccosolv), methanol (100 %, VWR Chemicals) were degassed by Ar bubbling and stocked in the glove-box. The Co precursor [$Co\{N(SiMe_3)_2\}_2(thf)$] was purchased from NanoMeps. The few-layer graphene (avanGRP 40) was purchased from Avanzare.

Synthesis of *hcp*-Co_{NR} and ε-Co_{NP}

In a Fisher-Porter bottle, HDA (819.3 mg, 3.4 mmol) dissolved in 16 mL toluene, was mixed with a solution of LA (420.1 mg, 2.1 mmol) in toluene (16 mL) and the mixture was stirred for 3 min. A green solution of [$Co\{N(SiMe_3)_2\}_2(thf)$], (902.3 mg, 2.0 mmol) in 8 mL toluene was then added under vigorous stirring to the LA-HDA mixture, giving rise to a dark blue solution. The Fischer-Porter bottle was sealed, removed from the glove box, pressurized with 3 bar of hydrogen and kept under stirring for 48 h in an oil bath preheated to 110°C. After this period of time, the excess of hydrogen was eliminated, the Fisher-Porter bottle was introduced in a glove box and the dark suspension was let to decant overnight. The black precipitate containing the *hcp*-Co_{NR} was washed several times with 10 mL toluene, until the supernatant became colorless and then with 10 mL pentane, and dried. The resulting powder was stored in the glove-box (ICP-OES: *hcp*-Co_{NR}: Co = 73.4 w%, elemental analysis: N = 0.18 w%). The brown supernatant containing the ε-Co_{NP} and ligand excess was collected and dried under vacuum. The as-obtained solid was then kept in the glove-box. (ICP-OES ε-Co_{NP}: Co = 0.64 w%, elemental analysis: N = 4.91 w%).

Purification of ε-Co_{NP} by repeated centrifugation steps of 15 min at 50000 rpm yielded ε-Co^*_{NP} samples (ICP-OES ε-Co^*_{NP}: Co = 57.2 w%, elemental analysis: N = 0.48 w%).

Catalyst preparation

The freestanding nanostructures were supported on oxidized commercially available few layer graphene.

Few layer graphene support functionalization

2 g of few-layer graphene (G) in 120 mL of HNO_3 (65%, VWR Chemicals) were heated at 100 °C for 3h. The mixture was then filtered and washed with deionized water until pH = 7. The final product (G_{ox}) was collected and dried at 80 °C overnight. It was then stored in the glove box.

Co immobilization on functionalized graphene

In a typical elaboration of a supported *hcp*-Co_{NR}/G_{ox} catalyst, 14 mg of powder containing *hcp*-Co_{NR} dispersed in 15 mL toluene were mixed with 200 mg of G_{ox} and sonicated for 10 min. After decantation the colorless supernatant was removed, the black solid washed three times with 20 mL toluene and dried, giving a powder which was stored in the glove-box. (ICP-OES: Co = 3.67 w%, elemental analysis: N < 0.01 w%).

In a typical elaboration of a ε-Co_{NP}/G_{ox} catalyst, 200 mg of G_{ox} were added in 60 mL of toluene in which were suspended 1.263 g of the powder containing the ε-Co_{NP} powder. The suspension was sonicated for 10 min and let to decant overnight under inert atmosphere. The light grey supernatant was removed, and the solid was washed three times with 20 mL toluene, dried, and stored in the glove-box. (ICP-OES: Co = 4.49 w%, elemental analysis: N =0.28 w%). The same procedure was used for the immobilization of ε-Co^*_{NP} on G_{ox} to give ε-Co^*_{NP}/G_{ox}. (ICP-OES: Co = 4.48 w%, elemental analysis: N = 0.03 w%).

Catalytic tests

No H_2 treatment of the catalysts was performed prior to the catalysis. The autoclave was charged in the glovebox. All chemicals were degassed before using. For all catalytic runs the Co amount introduced in the autoclave was between 1 and 2.6 mg (the exact Co amounts used in the catalytic runs are given in Table 1). The catalyst, 442 mg of cinnamaldehyde, 167 mg of nonane and 25 mL of solvent were added in the autoclave and mixed vigorously. The autoclave was then sealed and taken out of the glovebox, purged three times with 3 bar H_2 and then filled with 20 bar H_2. The temperature was increased to 120 °C and the stirring speed was fixed at 1200 rpm. Samples were taken from the autoclave at regular intervals and were analyzed on a Perkin Elmer, Clarus 580 gas chromatograph equipped with an Elite-5MS capillary column (30 m × 0.32 × 0.25 μm) and with a flame ionization detector. The activity

was calculated on the basis of the exact mass weighted and the Co content measured by ICP analysis of each catalyst employed. The conversion and selectivity were calculated according to the following equations:

$Conv\% = (n_i - n_f)/n_i * 100\%$

$S_x\% = n_x/n_{prod} * 100\%$

n_i: mol of CAL introduced

n_f: mol of CAL remaining at the end of the reaction

n_x: mol of product x

n_{prod}: total number of moles of products

The activity was calculated from the following relationship:

Activity = $mol_{CAL}\ mol_{Co}^{-1}\ h^{-1}$

mol_{CAL}: mol of CAL converted

mol_{Co}: mol of Co amount introduced

Recycling of ε-Co_{NP}/G_{ox}

The first run of recycling of ε-Co_{NP}/G_{ox} in ethanol followed the same procedure as described above, except that after 2h reaction, the reactor was cooled down rapidly and re-introduced into the glovebox. The reactor was let still for 2h to let the catalyst decant. The supernatant (20 mL) was removed carefully. 442 mg of cinnamaldehyde, 167 mg of nonane and 20 mL of ethanol were added. The reactor was then sealed and taken out of the glovebox for the second run of recycling. The recycling was carried out six times. To calculate the loss of activity, the cinnamaldehyde conversion of the first run was set to 100%. The conversion of each run versus the first run was calculated as the activity drop percentage.

Calculation of the nano-object geometric specific surface area

The geometric specific surface areas (SSA) of the nanoparticles were calculated using the formula $SSA = S_{tot}/(d_{Co}.V)$, where S_{tot} = the surface of *hcp*-Co_{NR} or ε-Co_{NP}, V their volume and d_{Co} the density of Co (8.86 g cm^{-3}). The values for the *hcp*-Co_{NR} and ε-Co_{NP} samples were obtained by using the mean dimensions determined by TEM and assuming simple geometrical models, considering a spherical shape for the ε-Co_{NP} and a hexagonal prismatic shape for the *hcp*-Co_{NR}.

Characterization

The size and the morphology of the cobalt nano-objects were studied by transmission electronic microscopy (TEM). All samples for TEM and high-resolution TEM (HRTEM) were prepared by evaporating a drop of a diluted suspension in toluene on a carbon-coated copper grid. Conventional TEM characterizations were performed on a JEOL JEM 1011 CX-T electron microscope operating at 100 kV with a point resolution of 4.5 Å. The particle size distribution was determined through a manual measurement of enlarged micrographs from different areas of the TEM grid (at least 200 particles). HRTEM was performed on a JEM-ARM200F Cold FEG equipped with a GATAN ULTRASCAN CCD camera and having a 1.9 Å point resolution.

The X-ray diffraction (XRD) patterns were obtained from samples encapsulated between two Kapton® foils to avoid sample oxidation. The diffractograms were recorded on a PANalytical Empyrean diffractometer using Co-K_α radiation (λ = 0.1789 nm) at 45 kV and 40 mA. The ε-Co_{NP} powder contained an excessive amount of ligand that did not allow identification of the Co peaks. The XRD measurement for the crystal structure determination was performed on a sample purified from the large excess of residual native ligands (ε-Co^*_{NP}), using a Thermo Fisher Scientific Sorvall MTX150 micro-ultracentrifuge. Two centrifugation cycles were performed at 50 000 rpm for 15 minutes. This allowed crystal structure and crystallite size determination, even though the presence of residual ligands is still visible in the XRD diffractogram. The crystallite size was calculated using the Scherrer equation by analysis of the ε-Co (221) peak. The XRD diffractograms of the G_{ox} supported catalysts did not allow identification of the Co-peaks due to the low Co-content (about 5 w%).

Infrared spectra were recorded on the isolated solid of ε-Co_{NP}, on a Nicolet 6700 FT-IR spectrometer in the range 4000-500 cm^{-1} using a Smart Orbit ATR platform (diamond crystal). The *hcp*-Co_{NP} and ε-Co^*_{NP} spectra were recorded from samples obtained by depositing on a Ge wafer a few drops of a toluene suspension of the isolated solids and letting the solvent evaporate.

ICP-OES and elemental analyses were performed by KOLBE Mikroanalytisches Laboratorium on a Spectro Acros instrument and a "Elementar" Model "Vario Micro Cube" CHN analyzer, respectively. X-ray photoelectron spectroscopy (XPS) spectra were recorded from samples prepared by depositing on a Si wafer a few drops of a toluene suspension of the isolated solid of ε-Co_{NP}, and the solvent was fully evaporated. The spectra were recorded using a K-alpha plus system (Thermo Fisher Scientific, East-Grinstead, U.K.) fitted with a micro-focused and monochromatic Al K_α X-ray source (1486.6 eV, spot size of 400 μm). The

spectrometer pass energy was set to 150 and 40 eV for the survey and the narrow high-resolution regions, respectively.

The magnetic measurements were performed by a Vibrating Sample Magnetometer (VSM) for *hcp*-Co_{NR} and ε-Co^*_{NP} and by a Superconducting QUantum Interference Device (SQuID) for ε-Co_{NP}. The samples were prepared in the glove box. In order to confirm the absence of any oxidation on the *hcp*-Co_{NR} sample, the M(H) hysteresis loops were recorded from -6 T to +6 T at 300 K (after a zero-field cooling (ZFC) and after a field cooling (FC) under +6 T) at 5 K. No Co/CoO exchange bias was detected at 5 K after the FC process. The same procedure was followed for ε-Co_{NP} and ε-Co^*_{NP}, with the only difference of the applied field intensity (-5 T to +5 T).

Results and Discussion

Co_{NR} of 97.9 ± 9.4 nm mean length and 5.9 ± 0.6 nm mean diameter (Figure 1a) and isotropic Co_{NP} of 6.5 ± 1.0 nm mean diameter (Figure 1b) are produced simultaneously, by reduction of Co/LA/HDA solutions.[43] Post-synthesis selective precipitation allows separation of the Co_{NR} from the Co_{NP}. The Co_{NR}, which have been characterized in previous publications, can be easily purified after isolation.[43,46] They adopt the *hcp* phase and they expose $\{11\bar{2}0\}$ type facets laterally and {0002} facets at their extremities. The Co_{NP} were isolated by complete evaporation of the reaction supernatant after Co_{NR} removal. The as obtained Co_{NP} fraction is mainly composed of organic products (99.4 w %). In agreement with previous analyses on Co_{NR},[46] this residue mainly consists in hexadecylammonium laurate and N-hexadecyl laurylamide, resulting from the condensation between LA and HDA during the nano-object synthesis. This was confirmed by IR and X-ray photoelectron spectroscopy (XPS) analyses of the powder containing the Co_{NP} and the native ligand matrix (Fig S1a-c). A fraction of the Co_{NP} sample was centrifuged to remove the majority of the organic residue yielding Co^*_{NP}. The IR spectra of the Co_{NR} and the Co*NP show that the ligands are the same in both cases (Figure S1d). The synthesis and the purification procedure are outlined in Scheme 1.

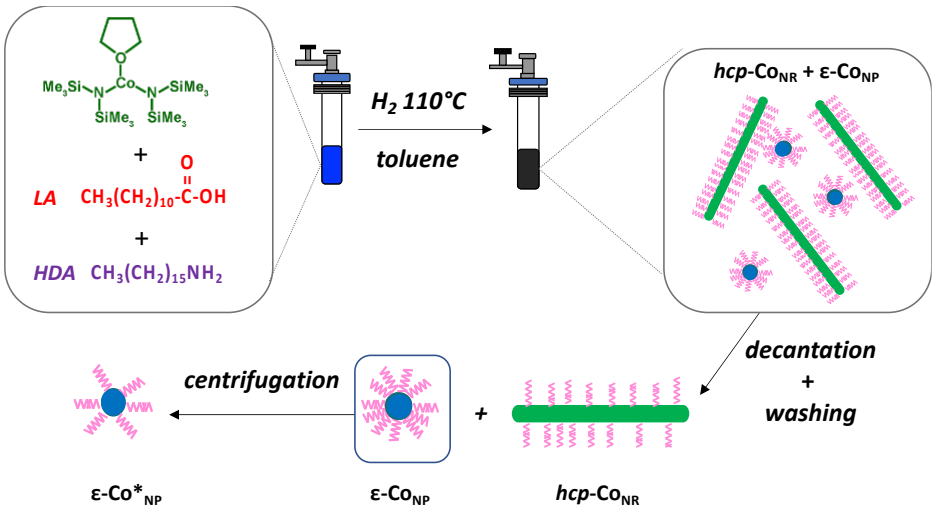

Scheme 1. Outline of the synthesis and the isolation of the Co nano-objects.

Interestingly, while the Co_{NR} crystallize in the *hcp* phase[43] (Fig. S2), the spherical Co_{NP} (Figure 1c) adopt the ε crystal structure, as evidenced by X-ray diffraction (XRD) of the purified ε-Co^*_{NP} (Figure 1d). In agreement with TEM data, the crystallite size was calculated to be 6.5 nm using the Scherrer equation, which confirms the single-crystal structure. Their spherical shape indicates that they are enclosed by facets of different types, albeit, of completely different symmetry than the facets exposed by the *hcp*-Co_{NR}. Magnetic measurements evidenced the absence of surface oxidation (Fig. S3). Indeed, the hysteresis loops measured after the field cooling (FC) procedure from 300 K down to 5 K under a magnetic field remain symmetric, which is a clear indication that no Co oxide layer is present on the surface of the nano-objects.

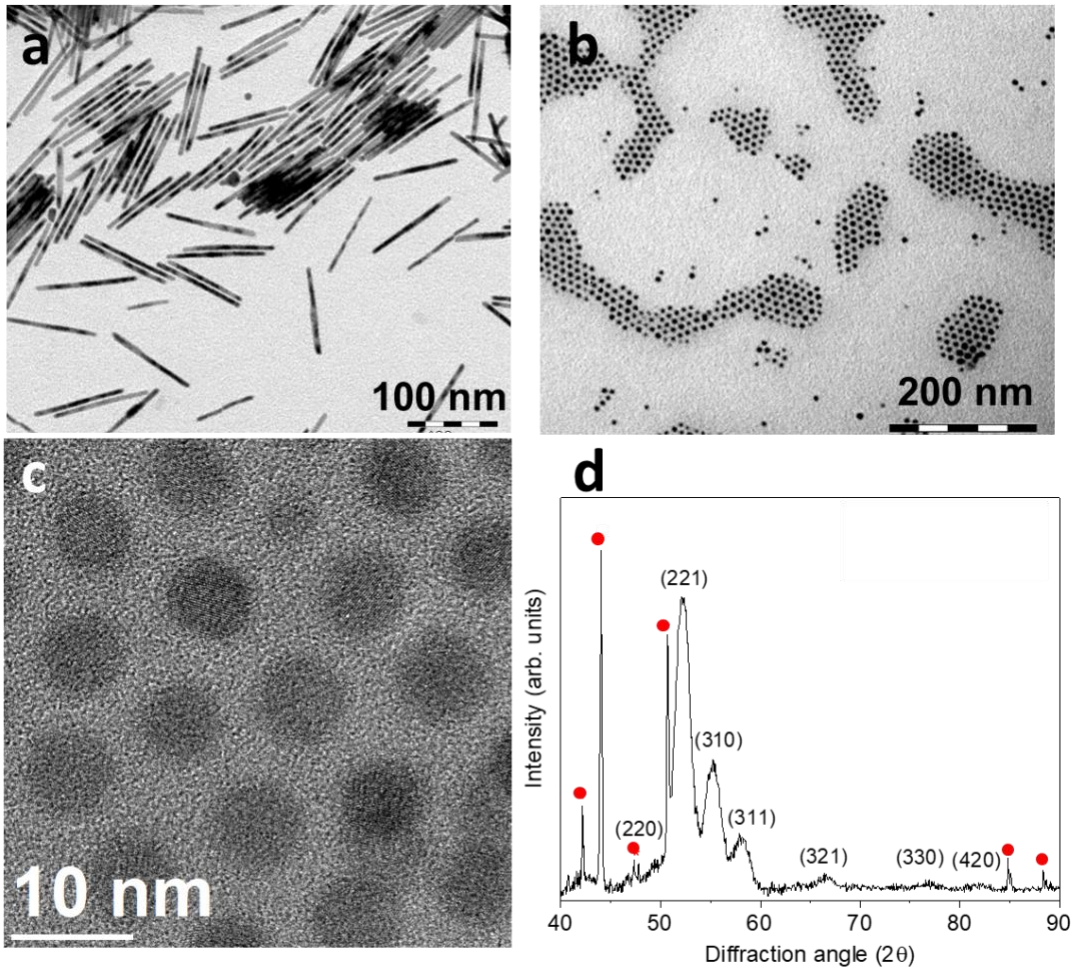

Figure 1. Cobalt nano-objects. TEM of (a) *hcp*-Co$_{NR}$ and (b) ε-Co$_{NP}$. (c) Higher magnification view of ε-Co$_{NP}$. (d) XRD pattern of the ε-Co*$_{NP}$. The peaks marked with a red mark are due to the ligand residues (Fig. S4).

The fact that nano-objects of two different structures could be isolated from the same synthesis, offered the opportunity to compare their catalytic performances without having to address the additional role that ligands of different nature may play.

The catalytic performances of freestanding *hcp*-Co$_{NR}$ and ε-Co$_{NP}$ were evaluated in the selective hydrogenation of CAL at 120 °C and 20 bar of H_2. Dioxane was the first solvent used, in order to avoid the formation of acetal by-products usually produced in alcohols from the acid-catalyzed condensation reaction between CAL (or HCAL) and the solvent.[38]

In Figure 2 and Table 1 we report the catalytic performances of the catalysts tested. Despite the lower geometric specific surface area of *hcp*-Co$_{NR}$ (89.2 $m^2.g^{-1}$) as compared to ε-Co$_{NP}$ 104 $m^2.g^{-1}$), the *hcp*-Co$_{NR}$ were more active than the ε-Co$_{NP}$, but the selectivity towards COL (at iso-conversion 40%) was higher for the ε-Co$_{NP}$ (86.8 % versus 66.7% for *hcp*-Co$_{NR}$).

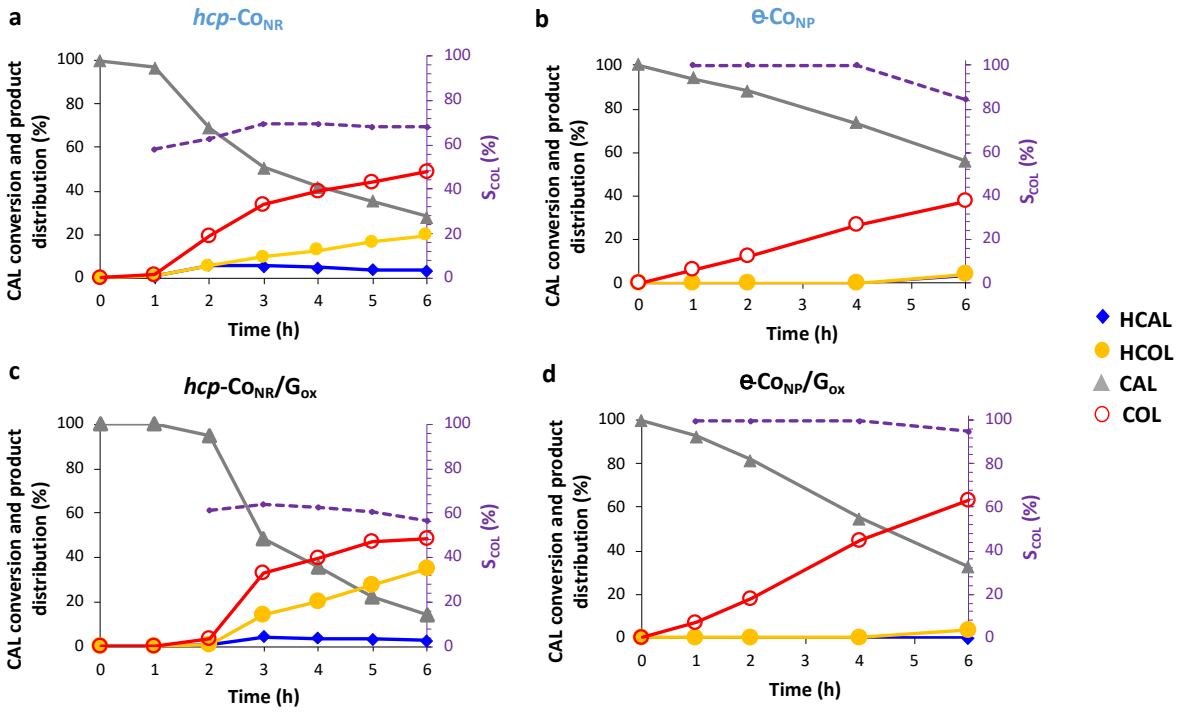

Figure 2. Catalytic performances in dioxane. (a) Freestanding *hcp*-Co_{NR}; (b) freestanding *ε*-Co_{NP}; (c) *hcp*-Co_{NR}/G_{ox} and (d) *ε*-Co_{NP}/G_{ox}.

Table 1. Hydrogenation of cinnamaldehyde catalyzed by Co catalysts (120 °C, P_{H2} = 20 bar).

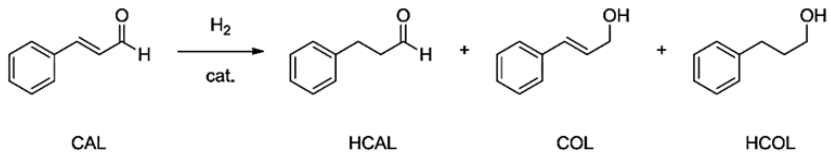

Catalyst	Co (10^{-2} mmol)	Co/N[a] (atomic)	Solvent	Conversion[b] (%)	Activity[c] (h^{-1})	Selectivity[c] (%)			
						COL	HCAL	HCOL	Acetal
hcp-Co_{NR}	3.6	96.8	Dioxane	59.7	16.6	66.7	16.2	17.1	0
ε–Co_{NP}	1.7	0.03	Dioxane	26.8	11.7	86.8 100[e]	7.8	5.4	0
ε-Co^*_{NP}[d]	4.5	28.3	Dioxane	19.1	4.3[e]	83.5[e]	8.9[e]	7.6[e]	0[e]
hcp-Co_{NR}/G_{ox}	3.1	NE[f]	Dioxane	64.0	19.3	66.7	9.7	23.6	0
ε-Co_{NP}/G_{ox}	3.1	3.8	Dioxane	45.1	10.8	100	0	0	0
ε-Co^*_{NP}/G_{ox}	4.4	35.5	Dioxane	38.4	7.0	75.8	14.8	9.6	0
ε-Co_{NP}/G_{ox}	3.1	3.8	Methanol	92.5	57	28.6	0	0	71.4
ε–Co_{NP}/G_{ox}	3.1	3.8	Ethanol	53.7	28.4	95.0	0	0	5.0

a) obtained from ICP and elemental analyses of Co and N respectively, b) at 4 h reaction; c) activity (mol_{CAL} mol_{Co}^{-1} h^{-1}) and selectivity at 40% conversion; d) *ε*-Co^*_{NP} are *ε*–Co_{NP} purified from the

ligand excess; e) data given at 30% conversion; f) NE = not estimated, N w% was below detection limit.

These results can be rationalized either by considering a different intrinsic performance of the two Co nano-objects, or by considering that the ligands, which are in high excess in the case of ε-Co$_{NP}$ (Co/N atomic ratio = 0.03) as compared to *hcp*-Co$_{NR}$ (Co/N atomic ratio = 96.8), reduce the activity of ε-Co$_{NP}$ because they block numerous active sites, and at the same time increase their selectivity to COL. While for Co catalysts there are no dedicated studies in the literature, a positive influence of long chain amine ligands on the selectivity to COL has been reported for Pt based catalysts.[47,48] In order to estimate the influence of the initial ligand coverage on ε-Co$_{NP}$, we also tested a purified fraction of the ε-Co$_{NP}$ sample (ε-Co*$_{NP}$), which presented the same particle size (Fig. S5) but much higher metal content (Co/N atomic ratio = 28.3). The activity (Figure 3a), but also the selectivity (Figure 3b) of ε-Co*$_{NP}$ are significantly lower than the ones of the ε-Co$_{NP}$. The activity decrease upon ligand partial elimination could be rationalized by an influence of ligand ordering on the NP surface (2D versus 3D ordering), as already reported for Pd$_{NP}$ hydrogenation catalysts.[20] In that case, the authors also showed that ordering on the NP surface is highly dependent not only on the ligand concentration but also on the ligand nature. Indeed, ligands containing ionic groups, are subjected to conformation changes depending on their concentration. Such an effect could also account for the significantly lower activity observed by the ε-Co*$_{NP}$ as compared to the ε-Co$_{NP}$. As far as selectivity is concerned, the most probable explanation is that in the case of ε-Co$_{NP}$ a 3D ordering of the ligands induces a higher COL selectivity due to the favorable orientation of the C=O group of CAL and its preferential adsorption.[47,48] The *hcp*-Co$_{NR}$, which present a higher activity have the lowest ligand content and present a lower selectivity as could be expected. However, their significantly higher activity despite their lower ligand content and their lower surface area points towards the conclusion that *hcp*-Co$_{NR}$ are inherently more active. It has to be noted that this does not mean that the *hcp* phase is generally a more active phase, but that the $\{11\bar{2}0\}$ facets, which constitute the majority of the *hcp*-Co$_{NR}$ exposed facets are more active than the facets of the ε-Co$_{NP}$. All freestanding *hcp*-Co$_{NR}$, ε-Co$_{NP}$ and ε-Co*$_{NP}$ are affected under the catalytic reaction conditions. Indeed, TEM observation of the crude reaction media after catalysis revealed the presence of Co$_{NP}$ of about 13 nm size for ε-Co$_{NP}$, agglomeration for ε-Co*$_{NP}$, while the Co$_{NR}$ appear more agglomerated and slightly corroded (Fig. S6).

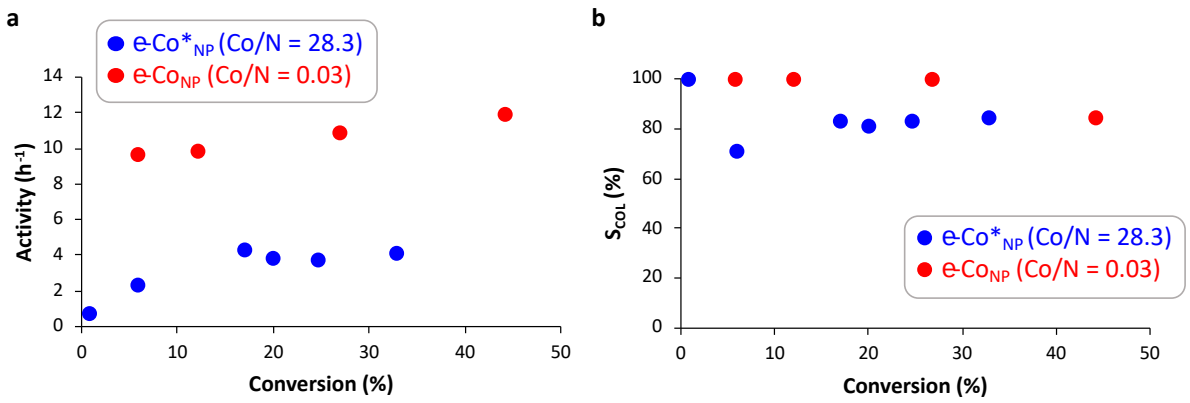

Figure 3. Comparison of the catalytic performances of ε-Co$_{NP}$ and ε-Co*$_{NP}$; (a) activity and (b) selectivity to COL.

As NP separation is tedious, immobilization on appropriate supports of colloidal NPs appears as the best approach to ensure optimized performance, stability and easy catalyst separation.[49] In parallel, immobilization should result in elimination of the surfactant excess, thanks to ligand displacement. In this context, *hcp*-Co$_{NR}$ and ε-Co$_{NP}$ were immobilized on few-layer graphene (G), which had been previously functionalized through treatment with HNO_3 to produce G$_{ox}$. This treatment produces oxygen containing functions (mainly carboxylic and phenolic),[50] which favor the immobilization of the nano-objects on the G$_{ox}$ support. A 5 w% nominal Co loading was targeted through mixing in toluene the freestanding Co$_{NR}$ and ε-Co$_{NP}$ with the G$_{ox}$ at room temperature. After immobilization and washing, the ICP analyses of *hcp*-Co$_{NR}$/G$_{ox}$ and ε-Co$_{NP}$/G$_{ox}$ showed Co loadings of 3.7 and 4.5 w%, respectively. The Co/N atomic ratios were 0.03 and 3.8 for ε-Co$_{NP}$ and ε-Co$_{NP}$/G$_{ox}$, respectively. Therefore, upon immobilization of the ε-Co$_{NP}$, a significant part of the residual ligand is eliminated. The Co/N atomic ratio in *hcp*-Co$_{NR}$/G$_{ox}$ could not be calculated since nitrogen content was lower than the detection limit (0.01%). Therefore, a higher amount of ligand for ε-Co$_{NP}$ is still present even on the supported catalysts. The nano-objects were well-dispersed on the G$_{ox}$ as shown in the TEM images on Figure 4.

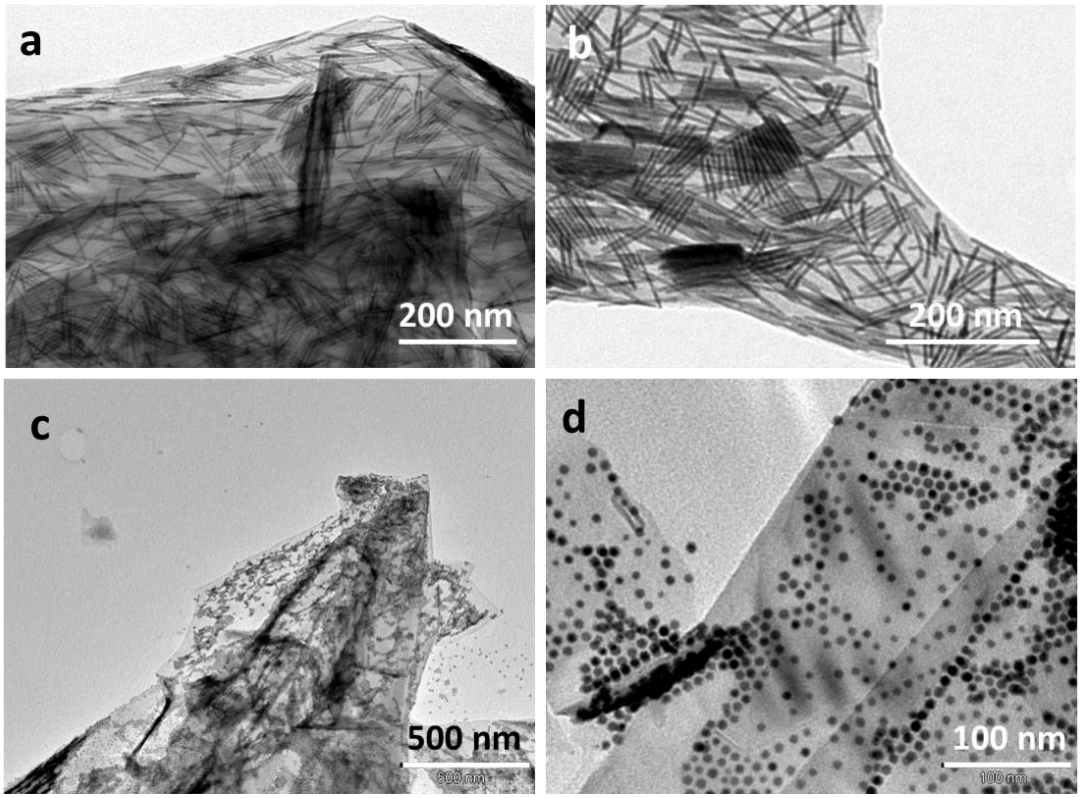

Figure 4. Supported cobalt nano-objects. TEM of (a), (b) *hcp*-Co_{NR}/G_{ox} and (c), (d) ε-Co_{NP}/G_{ox}.

Immobilization of the *hcp*-Co_{NR} on G_{ox} has no pronounced effect on their activity and selectivity to COL (Table 1). Globally, the immobilization allows reaching slightly higher activity (Figure 5a). XRD is not conclusive concerning the conservation of the structure after catalysis, because the G_{ox} exhibits strong reflections in the same 2θ range as the Co peaks (Fig. S7). However, TEM observation of the spent *hcp*-Co_{NR}/G_{ox} catalyst shows that nanorod morphology is not impacted after 6 hours of reaction and that the *hcp* structure is conserved. (Fig. S8)

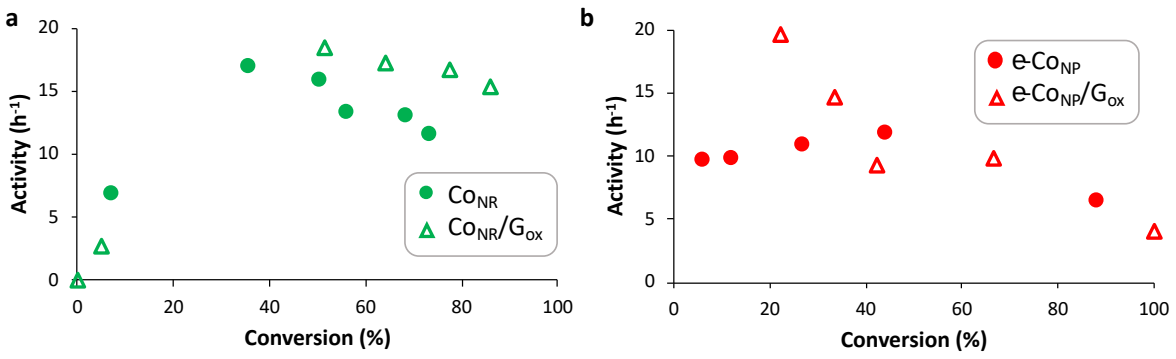

Figure 5. Comparison of the activity of freestanding and G_{ox} supported nanoparticles: (a) *hcp*-Co_{NR} and (b) ε-Co_{NP}.

On the other hand, for the ε-Co_{NP}/G_{ox} catalyst the initial activity is increased (Figure 5b) and the selectivity to COL reaches 100 % at 40 % conversion (Figure 2d and Table 1). If our assumption is correct that besides the Co structure, a 2D versus 3D ligand ordering also controls activity, and if for the 3.8 Co/N ratio the 3D ordering is still operative, it is logic that the ε-Co_{NP}/G_{ox} catalyst, which presents a higher Co/N ratio than the ε-Co_{NP} catalyst, is more active.

Furthermore, the NPs on the ε-Co_{NP}/G_{ox} catalyst seem to be intact even after complete CAL conversion, their size (6.1±1.2 nm) remaining practically unmodified. (Fig S9). Therefore, upon immobilization, ε-Co_{NP} double their initial activity and improve their selectivity, while no significant change is noticed for *hcp*-Co_{NR}. Furthermore, and as for freestanding nano-objects, the supported *hcp*-Co_{NR} are more active and less selective than the supported ε-Co_{NP} nano-objects.

We also investigated the reactivity of the ε–Co^*_{NP}/G_{ox} catalyst, which present a higher Co/N ratio compared to the ε-Co_{NP}/G_{ox} catalyst (35.4 and 3.8, respectively). As for the unsupported samples, we found that the sample with less ligand is globally less active and less selective (Figure 6).

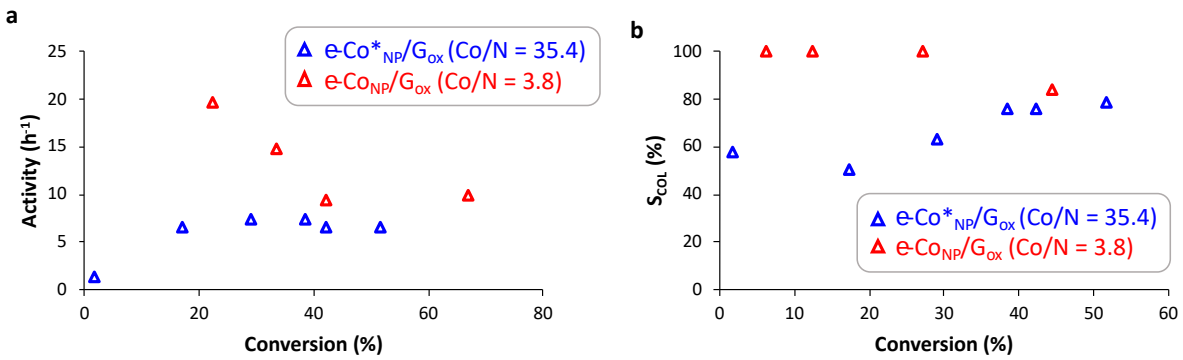

Figure 6. Comparison of ε-Co_{NP}/G_{ox} and ε-Co^*_{NP}/G_{ox} catalysts: (a) activity and (b) selectivity to COL.

Finally, we cannot discard the influence of confinement effects on the catalytic performances of ε-Co_{NP} upon immobilization.[51-53] Indeed, while the elemental and ICP analyses clearly show a large increase in the Co/N atomic ratio upon immobilization of the ε-Co_{NP} (from 0.03 to 3.8), in agreement with a decrease in the ligand residues on the supported catalyst, XPS analyses showed Co/N atomic ratios of 1.21 for ε-Co_{NP} and 0.38 for ε-Co_{NP}/G_{ox}.

This result is consistent with a partial confinement of ε-Co$_{NP}$ between the G$_{ox}$ layers and ligand residue adsorption on the surface of the support and could explain the very higher selectivity of the ε-Co$_{NP}$ upon immobilization.

To summarize, several parameters including the crystallographic phase of the metal, the ligand coverage and the possible confinement of the cobalt must be at the origin of the excellent results obtained with the ε-Co$_{NP}$/G$_{ox}$ system. Since the ligand coverage is often advanced as a key parameter in this type of catalysis, we have attempted to correlate the Co/N ratio with the catalytic performance (Fig. S10). It can be seen from Fig. S10a and 10b that no simple correlation exists between this ratio and the activity or selectivity of cobalt. Overall, it emerges that *hcp*-Co$_{NR}$ seem more active and less selective than ε-Co$_{NP}$, which could be related to the specific activity of the facets exposed in each case.

The results obtained with the ε-Co$_{NP}$/G$_{ox}$ catalyst are very encouraging as tentatively compared to the data reported in the literature for pure cobalt catalysts, even if the conditions under which the reactions have taken place are not the same. (Table S1). This prompted us to investigate alternative solvents, since it has been shown that alcohols can be beneficial in terms of activity in the case of cobalt catalysts.[38] In methanol, a large activity increase is noticed, however, acetal formation is very high (Table 1). Ethanol constitutes a better choice, leading to very high activity and COL selectivity with limited acetal production (Fig. S11 and Table 1). Figure 7a shows the evolution of activity and selectivity with conversion for ε-Co$_{NP}$/G$_{ox}$ and the results of recyclability tests are shown in Figure 7b. TEM and HRTEM images of the catalyst after recycling are shown in (Fig. S12). While low catalyst loading has not allowed confirming the conservation of the ε-structure by XRD after the catalytic runs, HRTEM on a ε-Co$_{NP}$ after recycling points toward the conservation of the ε-phase (Fig. S12b). Remarkably, the ε-Co$_{NP}$/G$_{ox}$ catalyst achieves high COL selectivity (> 85%) even at complete CAL conversion, while maintaining a catalytic activity comparable to some Ru catalysts presenting significantly lower COL selectivity.[54] These latter results place the ε-Co$_{NP}$/G$_{ox}$ catalyst largely above all the catalysts based on pure cobalt reported in the literature (Table S1 and Fig. S13).

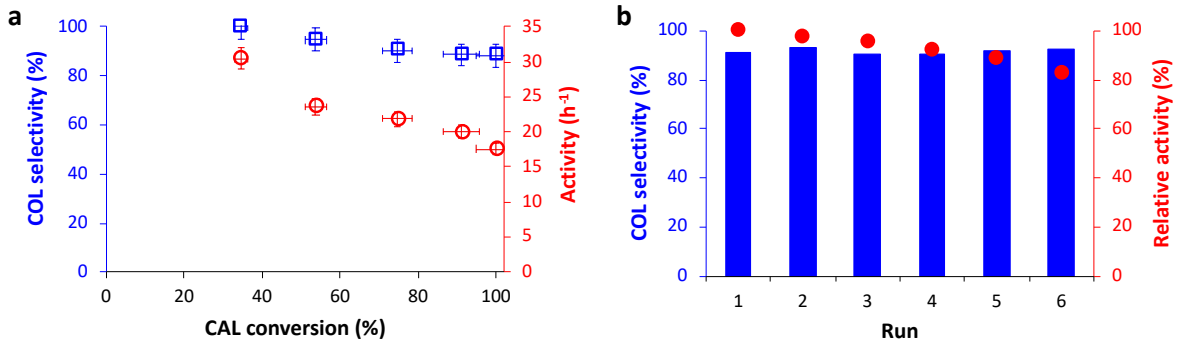

Figure 7. ε-CoNP/Gox catalyst performances in ethanol. Evolution of (a) the selectivity to COL and the activity as a function of conversion and (b) the selectivity to COL and the activity during recycling.

Conclusion

We have shown that metallic Co nano-objects prepared by an organometallic route are active catalysts for the selective hydrogenation of cinnamaldehyde to cinnamylalcohol. In particular, ε-CoNP supported on oxidized few-layer graphene, outperform their counterparts reported so far in the literature. Their good stability under the reaction conditions, and the higher selectivity as compared to the *hcp*-CoNR point towards a positive role of the largely unexplored in catalysis ε-Co structure. At this point, it would be premature to attribute the differences in the performances of the two types of nano-objects only to their different structure and further studies combining experiment and theory will allow determining the underlying reasons of their different performances.

Acknowledgements

D. Yi, K. S. and P. S. thank the EUR grant NanoX n° ANR-17- EURE-0009 for financial support in the framework of the "Programme des Investissements d'Avenir" through the project. Y. M., B. M., A. M., P-F. F., T. B., G. V., and K.S. also thank the European Union's Horizon 2020 research and innovation program for financial support of the SWIMMOT project under grant agreement No 899612. The authors thank Simon Cayez, Angélique Gillet and Adeline Pham for technical support.

ASSOCIATED CONTENT

Supporting Information

IR of *hcp*-Co_{NR}, ε-Co_{NP}, ε-Co^*_{NP} and XPS of ε-Co_{NP},, XRD and VSM of *hcp*-Co_{NR}, ε-Co_{NP} and ε-$Co^*_{NP,}$ TEM of ε-Co^*_{NP}, TEM of spent freestanding catalysts, XRD of fresh and spent *hcp*-Co_{NR}/Gox compared to Gox and *hcp*-Co_{NR}, TEM and HRTEM of spent *hcp*-Co_{NR}/G_{ox} , correlation between Co/N ratio and activity and selectivity of *hcp*-Co_{NR} and ε-Co_{NP}, comparison of the catalysts presented here and catalysts in the literature, comparison of catalytic performances in dioxane and ethanol of ε-Co_{NP}/Gox, TEM and HRTEM of ε-Co_{NP}/Gox after recycling.

AUTHOR INFORMATION

Corresponding Authors

Katerina Soulantica-Université de Toulouse, LPCNO CNRS, INSA, UPS UMR 5215, 31077 Toulouse, France;
orcid.org/0000-0003-3033-1620; Email: ksoulant@insa-toulouse.fr

Philippe Serp-LCC, CNRS-UPR 8241, ENSIACET, Université de Toulouse, France;
orcid.org/0000-0003-1424-2724 Email: philippe.serp@ensiacet.fr

Author Contributions

The manuscript was written through contributions of all authors. All authors have given approval to the final version of the manuscript.

References

(1) Soulantica, K.; Wetz, F.; Maynadié, J.; Falqui, A.; Tan, R. P.; Blon, T.; Chaudret, B.; Respaud, M. Magnetism of Single-Crystalline Co Nanorods. *Appl. Phys. Lett.* **2009**, *95*, 152504.
(2) Anagnostopoulou, E.; Grindi, B.; Lacroix, L.-M.; Ott, F.; Panagiotopoulos, I.; Viau, G. Dense Arrays of Cobalt Nanorods as Rare-Earth Free Permanent Magnets. *Nanoscale* **2016**, *8*, 4020–4029.
(3) Braik, M.; Sow, I.; Nelayah, J.; Belkhir, A.; Faustini, M.; Mercone, S.; Nowak, S.; Decorse, P.; Piquemal, J.-Y.; Félidj, N. Introducing Cobalt as a Potential Plasmonic Candidate Combining Optical and Magnetic Functionalities within the Same Nanostructure. *Nanoscale* **2021**, *13*, 2639–2647.
(4) Khodakov, A. Y.; Chu, W.; Fongarland, P. Advances in the Development of Novel Cobalt Fischer−Tropsch Catalysts for Synthesis of Long-Chain Hydrocarbons and Clean Fuels. *Chem. Rev.* **2007**, *107*, 1692–1744.
(5) de la Peña O'Shea, V. A.; Moreira, I. de P. R.; Roldán, A.; Illas, F. Electronic and Magnetic Structure of Bulk Cobalt: The α, β, and ε-Phases from Density Functional Theory Calculations. *J. Chem. Phys.* **2010**, *133*, 024701.

(6) Dinega, D. P.; Bawendi, M. G. A Solution-Phase Chemical Approach to a New Crystal Structure of Cobalt. *Angew. Chem. Int. Ed.* **1999**, *38*, 1788–1791.
(7) Sun, S.; Murray, C. B. Synthesis of Monodisperse Cobalt Nanocrystals and Their Assembly into Magnetic Superlattices. *J. Appl. Phys.* **1999**, *85*, 4325–4330.
(8) Liu, J.-X.; Li, W.-X. Theoretical Study of Crystal Phase Effect in Heterogeneous Catalysis. *WIREs Comput. Mol. Sci.* **2016**, *6*, 571–583.
(9) Fan, Z.; Zhang, H. Template Synthesis of Noble Metal Nanocrystals with Unusual Crystal Structures and Their Catalytic Applications. *Acc. Chem. Res.* **2016**, *49*, 2841–2850.
(10) Yao, Y.; He, D. S.; Lin, Y.; Feng, X.; Wang, X.; Yin, P.; Hong, X.; Zhou, G.; Wu, Y.; Li, Y. Modulating Fcc and Hcp Ruthenium on the Surface of Palladium–Copper Alloy through Tunable Lattice Mismatch. *Angew. Chem. Int. Ed.* **2016**, *55*, 5501–5505.
(11) Ghosh, S.; Jagirdar, B. R. Effect of the Crystallographic Phase of Ruthenium Nanosponges on Arene and Substituted-Arene Hydrogenation Activity. *ChemCatChem* **2018**, *10*, 3086–3095.
(12) Li, S.; Dong, M.; Peng, M.; Mei, Q.; Wang, Y.; Yang, J.; Yang, Y.; Chen, B.; Liu, S.; Xiao, D.; Liu, H.; Ma, D.; Han, B. Crystal-Phase Engineering of PdCu Nanoalloys Facilitates Selective Hydrodeoxygenation at Room Temperature. *The Innovation* **2022**, *3*, 100189.
(13) Liu, J.-X.; Su, H.-Y.; Sun, D.-P.; Zhang, B.-Y.; Li, W.-X. Crystallographic Dependence of CO Activation on Cobalt Catalysts: HCP versus FCC. *J. Am. Chem. Soc.* **2013**, *135*, 16284–16287.
(14) Liu, J.-X.; Wang, P.; Xu, W.; Hensen, E. J. M. Particle Size and Crystal Phase Effects in Fischer-Tropsch Catalysts. *Engineering* **2017**, *3*, 467–476.
(15) van Deelen, T. W.; Su, H.; Sommerdijk, N. A. J. M.; de Jong, K. P. Assembly and Activation of Supported Cobalt Nanocrystal Catalysts for the Fischer–Tropsch Synthesis. *Chem. Commun.* **2018**, *54*, 2530–2533.
(16) Somorjai, G. A.; Li, Y. Selective Nanocatalysis of Organic Transformation by Metals: Concepts, Model Systems, and Instruments. *Top. Catal.* **2010**, *53*, 832–847.
(17) Dai, Y.; Wang, Y.; Liu, B.; Yang, Y. Metallic Nanocatalysis: An Accelerating Seamless Integration with Nanotechnology. *Small* **2015**, *11*, 268–289.
(18) Witte, P. T.; Berben, P. H.; Boland, S.; Boymans, E. H.; Vogt, D.; Geus, J. W.; Donkervoort, J. G. BASF NanoSelect^{TM} Technology: Innovative Supported Pd- and Pt-Based Catalysts for Selective Hydrogenation Reactions. *Top. Catal.* **2012**, *55*, 505–511.
(19) Liu, K.; Qin, R.; Zheng, N. Insights into the Interfacial Effects in Heterogeneous Metal Nanocatalysts toward Selective Hydrogenation. *J. Am. Chem. Soc.* **2021**, *143*, 4483–4499.
(20) Albani, D.; Vilé, G.; Mitchell, S.; Witte, P. T.; Almora-Barrios, N.; Verel, R.; López, N.; Pérez-Ramírez, J. Ligand Ordering Determines the Catalytic Response of Hybrid Palladium Nanoparticles in Hydrogenation. *Catal. Sci. Technol.* **2016**, *6*, 1621–1631.
(21) Chen, G.; Xu, C.; Huang, X.; Ye, J.; Gu, L.; Li, G.; Tang, Z.; Wu, B.; Yang, H.; Zhao, Z.; Zhou, Z.; Fu, G.; Zheng, N. Interfacial Electronic Effects Control the Reaction Selectivity of Platinum Catalysts. *Nat. Mater.* **2016**, *15*, 564–569.
(22) Wu, D.; Baaziz, W.; Gu, B.; Marinova, M.; Hernández, W. Y.; Zhou, W.; Vovk, E. I.; Ersen, O.; Safonova, O. V.; Addad, A.; Nuns, N.; Khodakov, A. Y.; Ordomsky, V. V. Surface Molecular Imprinting over Supported Metal Catalysts for Size-Dependent Selective Hydrogenation Reactions. *Nat. Catal.* **2021**, *4*, 595–606.
(23) Zhang, X.; Liu, H.; Shi, Y.; Han, J.; Yang, Z.; Zhang, Y.; Long, C.; Guo, J.; Zhu, Y.; Qiu, X.; Xue, G.; Zhang, L.; Zhang, B.; Chang, L.; Tang, Z. Boosting CO2 Conversion

with Terminal Alkynes by Molecular Architecture of Graphene Oxide-Supported Ag Nanoparticles. *Matter* **2020**, *3*, 558–570.
(24) Lan, X.; Wang, T. Highly Selective Catalysts for the Hydrogenation of Unsaturated Aldehydes: A Review. *ACS Catal.* **2020**, *10*, 2764–2790.
(25) Luneau, M.; Lim, J. S.; Patel, D. A.; Sykes, E. C. H.; Friend, C. M.; Sautet, P. Guidelines to Achieving High Selectivity for the Hydrogenation of α,β-Unsaturated Aldehydes with Bimetallic and Dilute Alloy Catalysts: A Review. *Chem. Rev.* **2020**, *120*, 12834–12872.
(26) Tsang, S. C.; Cailuo, N.; Oduro, W.; Kong, A. T. S.; Clifton, L.; Yu, K. M. K.; Thiebaut, B.; Cookson, J.; Bishop, P. Engineering Preformed Cobalt-Doped Platinum Nanocatalysts For Ultraselective Hydrogenation. *ACS Nano* **2008**, *2*, 2547–2553.
(27) Zheng, Q.; Wang, D.; Yuan, F.; Han, Q.; Dong, Y.; Liu, Y.; Niu, X.; Zhu, Y. An Effective Co-Promoted Platinum of Co–Pt/SBA-15 Catalyst for Selective Hydrogenation of Cinnamaldehyde to Cinnamyl Alcohol. *Catal. Lett.* **2016**, *146*, 1535–1543.
(28) Su, J.; Shi, W.; Liu, X.; Zhang, L.; Cheng, S.; Zhang, Y.; Botton, G. A.; Zhang, B. Probing the Performance of Structurally Controlled Platinum-Cobalt Bimetallic Catalysts for Selective Hydrogenation of Cinnamaldehyde. *J. Catal.* **2020**, *388*, 164–170.
(29) Koo-amornpattana, W.; Winterbottom, J. M. Pt and Pt-Alloy Catalysts and Their Properties for the Liquid-Phase Hydrogenation of Cinnamaldehyde. *Catal. Today* **2001**, *66*, 277–287.
(30) Nitta, Y.; Hiramatsu, Y.; Imanaka, T. Effects of Preparation Variables of Supported-Cobalt Catalysts on the Selective Hydrogenation of α,β-Unsaturated Aldehydes. *J. Catal.* **1990**, *126*, 235–245.
(31) Joseph Antony Raj, K.; Prakash, M. G.; Elangovan, T.; Viswanathan, B. Selective Hydrogenation of Cinnamaldehyde over Cobalt Supported on Alumina, Silica and Titania. *Catal. Lett.* **2012**, *142*, 87–94.
(32) Wu, Z.; Zhao, J.; Zhang, M.; Li, W.; Tao, K. Synthesis of a Stable and Porous Co–B Nanoparticle Catalyst for Selective Hydrogenation of Cinnamaldehyde to Cinnamic Alcohol. *Catal. Commun.* **2010**, *11*, 973–976.
(33) Bailie, J. E.; Rochester, C. H.; Hutchings, G. J. IR Study of Acrolein Hydrogenation over Co/SiO_2 catalysts. *J. Chem. Soc. Faraday Trans.* **1997**, *93*, 4389–4394.
(34) Li, H.; Chen, X.; Wang, M.; Xu, Y. Selective Hydrogenation of Cinnamaldehyde to Cinnamyl Alcohol over an Ultrafine Co-B Amorphous Alloy Catalyst. *Appl. Catal. Gen.* **2002**, *225*, 117–130.
(35) Li, H.; Liu, J.; Xie, S.; Qiao, M.; Dai, W.; Li, H. Highly Active Co–B Amorphous Alloy Catalyst with Uniform Nanoparticles Prepared in Oil-in-Water Microemulsion. *J. Catal.* **2008**, *259*, 104–110.
(36) Rodrigues, E. L.; Bueno, J. M. C. Co/SiO_2 Catalysts for Selective Hydrogenation of Crotonaldehyde II: Influence of the Co Surface Structure on Selectivity. *Appl. Catal. Gen.* **2002**, *232*, 147–158.
(37) Ando, C.; Kurokawa, H.; Miura, H. Selective Hydrogenation of Aldehyde Groups in Various α,β-Unsaturated Aldehydes over Alumina-Supported Cobalt (0) Catalyst. *Appl. Catal. Gen***. 1999**, *185*, 181–183.
(38) Zhang, X. B.; Zhang, Y. J.; Chen, F.; Xiang, Y. Z.; Zhang, B.; Xu, L. Y.; Zhang, T. R. Efficient Selective Hydrogenation of Cinnamaldehyde over Zeolite Supported Cobalt Catalysts in Water. *React. Kinet. Mech. Catal.* **2015**, *115*, 283–292.

(39) Zhang, L.; Chen, X.; Li, C.; Armbrüster, M.; Peng, Z.; Liang, C. Cobalt Silicides Nanoparticles Embedded in N-Doped Carbon as Highly Efficient Catalyst in Selective Hydrogenation of Cinnamaldehyde. *ChemistrySelect* **2018**, *3*, 1658–1666.
(40) Bustamante, T. M.; Fraga, M. A.; Fierro, J. L. G.; Campos, C. H.; Pecchi, G. Cobalt SiO_2 Core-Shell Catalysts for Chemoselective Hydrogenation of Cinnamaldehyde. *Catal. Today* **2020**, *356*, 330–338.
(41) Lv, Y.; Han, M.; Gong, W.; Wang, D.; Chen, C.; Wang, G.; Zhang, H.; Zhao, H. Fe-Co Alloyed Nanoparticles Catalyzing Efficient Hydrogenation of Cinnamaldehyde to Cinnamyl Alcohol in Water. *Angew. Chem. Int. Ed.* **2020**, *59*, 23521–23526.
(42) Liakakos, N.; Cormary, B.; Li, X.; Lecante, P.; Respaud, M.; Maron, L.; Falqui, A.; Genovese, A.; Vendier, L.; Koïnis, S.; Chaudret, B.; Soulantica, K. The Big Impact of a Small Detail: Cobalt Nanocrystal Polymorphism as a Result of Precursor Addition Rate during Stock Solution Preparation. *J. Am. Chem. Soc.* **2012**, *134*, 17922–17931.
(43) Cormary, B.; Li, T.; Liakakos, N.; Peres, L.; Fazzini, P.-F.; Blon, T.; Respaud, M.; Kropf, A. J.; Chaudret, B.; Miller, J. T.; Mader, E. A.; Soulantica, K. Concerted Growth and Ordering of Cobalt Nanorod Arrays as Revealed by Tandem in Situ SAXS-XAS Studies. *J. Am. Chem. Soc.* **2016**, *138*, 8422–8431.
(44) Harmel, J.; Berliet, A.; Dembélé, K.; Marcelot, C.; Gay, A.-S.; Ersen, O.; Maury, S.; Fécant, A.; Chaudret, B.; Serp, P.; Soulantica, K. A Seed-Mediated Approach for the Preparation of Modified Heterogeneous Catalysts. *ChemCatChem* **2018**, *10*, 1614–1619.
(45) Harmel, J.; Peres, L.; Estrader, M.; Berliet, A.; Maury, S.; Fécant, A.; Chaudret, B.; Serp, P.; Soulantica, K. *Hcp* -Co Nanowires Grown on Metallic Foams as Catalysts for Fischer–Tropsch Synthesis. *Angew. Chem. Int. Ed.* **2018**, *57*, 10579–10583.
(46) Kaźmierczak, K.; Yi, D.; Jaud, A.; Fazzini, P.-F.; Estrader, M.; Viau, G.; Decorse, P.; Piquemal, J.-Y.; Michel, C.; Besson, M.; Soulantica, K.; Perret, N. Influence of Capping Ligands on the Catalytic Performances of Cobalt Nanoparticles Prepared with the Organometallic Route. *J. Phys. Chem. C* **2021**, *125*, 7711–7720.
(47) Wu, B.; Huang, H.; Yang, J.; Zheng, N.; Fu, G. Selective Hydrogenation of α,β-Unsaturated Aldehydes Catalyzed by Amine-Capped Platinum-Cobalt Nanocrystals. *Angew. Chem. Int. Ed.* **2012**, *51*, 3440–3443.
(48) Peres, L.; Axet, M. R.; Yi, D.; Serp, P.; Soulantica, K. Selective Hydrogenation of Cinnamaldehyde by Unsupported and Few Layer Graphene Supported Platinum Concave Nanocubes Exposing {110} Facets Stabilized by a Long-Chain Amine. *Catal. Today* **2020**, *357*, 166–175.
(49) Costa, N. J. S.; Rossi, L. M. Synthesis of Supported Metal Nanoparticle Catalysts Using Ligand Assisted Methods. *Nanoscale* **2012**, *4*, 5826.
(50) Contreras, R. C.; Guicheret, B.; Machado, B. F.; Rivera-Cárcamo, C.; Curiel Alvarez, M. A.; Valdez Salas, B.; Ruttert, M.; Placke, T.; Favre Réguillon, A.; Vanoye, L.; de Bellefon, C.; Philippe, R.; Serp, P. Effect of Mesoporous Carbon Support Nature and Pretreatments on Palladium Loading, Dispersion and Apparent Catalytic Activity in Hydrogenation of Myrcene. *J. Catal.* **2019**, *372*, 226–244.
(51) Mu, R.; Fu, Q.; Jin, L.; Yu, L.; Fang, G.; Tan, D.; Bao, X. Visualizing Chemical Reactions Confined under Graphene. *Angew. Chem. Int. Ed.* **2012**, *51*, 4856–4859.
(52) Deng, D.; Novoselov, K. S.; Fu, Q.; Zheng, N.; Tian, Z.; Bao, X. Catalysis with Two-Dimensional Materials and Their Heterostructures. *Nat. Nanotechnol.* **2016**, *11* (3), 218–230.
(53) Zhao, M.; Yuan, K.; Wang, Y.; Li, G.; Guo, J.; Gu, L.; Hu, W.; Zhao, H.; Tang, Z. Metal–Organic Frameworks as Selectivity Regulators for Hydrogenation Reactions. *Nature* **2016**, *539*, 76–80.

(54) Leng, F.; Gerber, I. C.; Axet, M. R.; Serp, P. Selectivity Shifts in Hydrogenation of Cinnamaldehyde on Electron-Deficient Ruthenium Nanoparticles. *Comptes Rendus Chim.* **2018**, *21*, 346–353.

TOC graphic